




ORIGINAL RESEARCH ARTICLE

# Thermoelectric Properties of Cobalt-Doped $\beta$ -FeSi<sub>2</sub> with SiC Nanoparticle Inclusions

HUI SUN <sup>1,4</sup> XU LU,<sup>2</sup> and DONALD T. MORELLI<sup>3</sup>

1.—Department of Basic Teaching, Anhui Institute of Information Technology, Wuhu 241000, Anhui, China. 2.—Department of Applied Physics, Chongqing University, Chongqing 401331, China. 3.—Department of Chemical Engineering and Materials Science, Michigan State University, East Lansing, MI 48824, USA. 4.—e-mail: 526263687@qq.com

Cobalt doping is an effective approach to improve the thermoelectric properties of semiconducting  $\beta$ -FeSi<sub>2</sub> materials. Through preparing  $\beta$ -Fe<sub>1-x</sub>Co<sub>x</sub>Si<sub>2</sub> samples with  $x$  ranging from 0.05 to 0.11, an enhanced  $ZT$  of about 0.35 could be achieved within quite a wide doping range (8 mol.% to 10 mol.%) at around 950 K. To further improve the thermoelectric performance, a composite structure consisting of a large grain matrix of  $\beta$ -Fe<sub>0.92</sub>Co<sub>0.08</sub>Si<sub>2</sub> and inert SiC nanoparticle inclusions was intentionally employed to reduce the lattice thermal conductivity. The microstructure and the effects on the thermoelectric properties of  $\beta$ -Fe<sub>0.92</sub>Co<sub>0.08</sub>Si<sub>2</sub> with various SiC nanoparticle concentrations were explored. The SiC nanoparticles could be well dispersed into the matrix material without significant agglomerations by the powder processing method. However, the thermal conductivity was not considerably reduced while the electrical properties were affected to some extent, resulting in no gain in the  $ZT$ . The current results show that it is feasible to prepare high-quality nanocomposites through the powder processing method, and enhanced thermoelectric performance is expected when using other chemically stable inclusions with lower thermal conductivity and smaller size.

**Key words:**  $\beta$ -FeSi<sub>2</sub>, cobalt doping, SiC nanoinclusions, powder processing, thermoelectric properties

## INTRODUCTION

Thermoelectric materials are used to achieve direct conversion between electricity and heat. The efficiency of thermoelectric materials is related to the dimensionless figure of merit  $ZT = S^2T/\rho\kappa$ , where  $S$  is the Seebeck coefficient,  $\rho$  is the electrical resistivity,  $\kappa$  is the thermal conductivity, and  $T$  is absolute temperature. Thus, promising thermoelectric materials are expected to possess low thermal conductivity but large power factor ( $S^2/\rho$ ).

Nowadays, most high-efficiency thermoelectric materials are based on expensive elemental constituents. This high manufacturing cost may restrict their large-scale application, despite the

higher conversion efficiencies. Considering the compromise between materials abundance and efficiency,  $\beta$ -FeSi<sub>2</sub> is one of the promising inexpensive materials for high-temperature power generation.<sup>1,2</sup> In 1964, the thermoelectric properties of  $\beta$ -FeSi<sub>2</sub> were studied by Ware and McNeill,<sup>3</sup> and its potential for power generation has been explored since then.

Semiconducting  $\beta$ -FeSi<sub>2</sub> shows an orthorhombic crystal structure (space group  $Cmca$ ). Its theoretical density is 4.93 g/cm<sup>3</sup>,<sup>4</sup> and the relatively low density is another advantage of this material. The nature of the electronic structures has not been elucidated yet, probably due to the intrinsic defects in  $\beta$ -FeSi<sub>2</sub>.<sup>5</sup> Experimental results showed a direct bandgap of 0.87 eV to 0.90 eV,<sup>6,7</sup> whereas theoretical calculations gave a narrower indirect gap of 0.44 eV to 0.78 eV.<sup>8–11</sup> The electrical properties can be tuned by  $p$ -type (e.g., Al at Si sites<sup>12</sup>) and  $n$ -type (e.g. Co, Ni, or

(Received December 22, 2020; accepted February 19, 2021; published online March 15, 2021)

Pt at Fe sites<sup>2,13–16</sup>) doping. In the past, the highest reported  $ZT$  value at around 900 K ranged from 0.19 to 0.42 for 6 mol.% Co-doped samples.<sup>17</sup> This large range in values stems completely from the difference in the high-temperature thermal conductivity measurements.

In this study, we tried to explore the electrical and thermal transport properties of Co-doped  $\beta$ -FeSi<sub>2</sub> materials more fully. Since the solubility limit of Co in  $\beta$ -FeSi<sub>2</sub> is reported to be as high as 12 mol.%,<sup>18</sup> dopant concentrations up to 11 mol.% were intentionally used to replace Fe atoms. Furthermore, the lattice thermal conductivity of Co-doped  $\beta$ -FeSi<sub>2</sub> is about two times that of state-of-the-art materials.<sup>19</sup> Therefore,  $ZT$  is expected to be further enhanced by reducing the lattice thermal conductivity. It is believed that intentionally formed nanocomposites can achieve electrical and thermal transport decoupling.<sup>20–23</sup> Since SiC is a chemically stable inclusion even at high temperatures, it is supposed to only scatter phonons and not affect the carrier concentration. Based on this idea, composites consisting of Co-doped  $\beta$ -FeSi<sub>2</sub> and SiC nanoparticles were investigated.

## EXPERIMENTAL PROCEDURES

Initial Fe<sub>1-x</sub>Co<sub>x</sub>Si<sub>2</sub> ( $x = 0.05$  to  $0.11$ ) ingots were prepared by arc melting stoichiometric quantities of high-purity Fe (99.95%, Alfa Aesar), Co (99.95%, Alfa Aesar), and Si (99.9999%, Alfa Aesar) elements on a water-cooled copper hearth under flowing argon. The ingots were flipped and remelted typically five times to encourage homogeneity. They were then sealed in quartz ampoules under vacuum ( $\sim 10^{-3}$  Pa) and annealed at 955°C for 3 days. There were always cracks inside the samples, thus an appropriate section could be obtained for transport property measurements. In this case, powder processing was employed to prepare high-quality samples. The standard synthesis procedure was to pulverize the arc-melted ingots for 30 min, press the powder under pressure of 30 MPa at temperature of 1150°C for 8 min to form a dense cylinder, and finally anneal the sealed samples at 800°C for 100 h. All the ingot pulverization was completed with an 8004 tungsten carbide vial set in a SPEX SamplePrep 8000M high-energy ball mill. The densification was achieved using a Pulsed electric current sintering (PECS) system from Thermal Technology LLC under argon atmosphere. To minimize oxidation, the vial set was sealed in an argon-filled glove box with barrier film before milling, and the powders were also loaded in a glove box and transferred to the PECS system quickly. The  $x = 0.08$  sample ( $\beta$ -Fe<sub>0.92</sub>Co<sub>0.08</sub>Si<sub>2</sub>) was selected as the control composition for the study of the composites with SiC nanoparticles ( $\beta$ -phase, 95% purity, 50 nm to 60 nm average particle size; NanoAmor) inclusions. The SiC nanoparticles were mixed with the  $\beta$ -Fe<sub>0.92</sub>Co<sub>0.08</sub>Si<sub>2</sub> powders and three composite

samples with SiC concentrations of 1 wt.%, 3 wt.%, and 5 wt.% (corresponding to 1.5 vol.%, 4.4 vol.%, and 7.1 vol.%, respectively) were prepared. All the dense pellets were sectioned into rectangular parallelepipeds with dimensions of  $\sim 2.5$  mm  $\times$  2.5 mm  $\times$  10 mm for electrical transport measurements and thin disks with thickness of  $\sim 1$  mm and diameter of  $\sim 12.7$  mm for thermal transport measurements.

The phase and crystal structure were determined by powder x-ray diffraction (XRD) analysis using a Rigaku Miniflex II desktop x-ray diffractometer with Cu K $\alpha$  (wavelength 0.154187 nm) radiation. The powders were obtained by crushing a portion of each sample with a set of agate mortar and pestle. The XRD patterns were evaluated using Jade 9.0 software, which includes a JCPDS XRD database.

The microstructures were observed by field-emission scanning electron microscopy (SEM; JEOL JSM-7500F). The chemical composition of the samples was determined by energy-dispersive x-ray spectroscopy (EDS). Backscattered electron (BSE) imaging was selected to distinguish minor phases from the majority.

The high-temperature electrical resistivity and Seebeck coefficient were simultaneously measured using a commercial ULVAC ZEM-3 system under low-pressure helium atmosphere. The high-temperature thermal conductivity was obtained based on the thermal diffusivity ( $D$ ), specific heat capacity ( $C_p$ ), and sample density ( $d$ ) measurements as  $\kappa = D \cdot C_p \cdot d$ . The thermal diffusivity and the specific heat capacity were measured using a commercial Netzsch LFA-457 laser flash system and a Netzsch DSC-200 F3 system, respectively. The room-temperature sample density was determined by the Archimedes method with ethanol as medium. All the pellets in this study possessed densities above 95% of the theoretical value.

## RESULTS AND DISCUSSION

As shown in Fig. 1, the XRD patterns only showed  $\beta$ -FeSi<sub>2</sub> single phase for all the samples. The presence of FeSi phase is a well-known issue affecting the purity of  $\beta$ -FeSi<sub>2</sub>.<sup>24–27</sup> This problem was avoided using our preparation method.

Figure 2 presents the XRD patterns of the  $\beta$ -Fe<sub>0.92</sub>Co<sub>0.08</sub>Si<sub>2</sub> and SiC composites. It can be seen that the  $\beta$ -FeSi<sub>2</sub> phase was formed in each sample. It is hard to observe the SiC phase because of its low intensity, caused by the small particle size and the low concentration.

Figure 3 shows BSE images of the control sample and the composites. A secondary dark phase is observed in all the composites, and its content increases with increasing SiC concentration. The chemical compositions of the gray and black phases in each sample were determined by EDS, and the results are presented in Table I. The gray region only shows the composition of the matrix material,

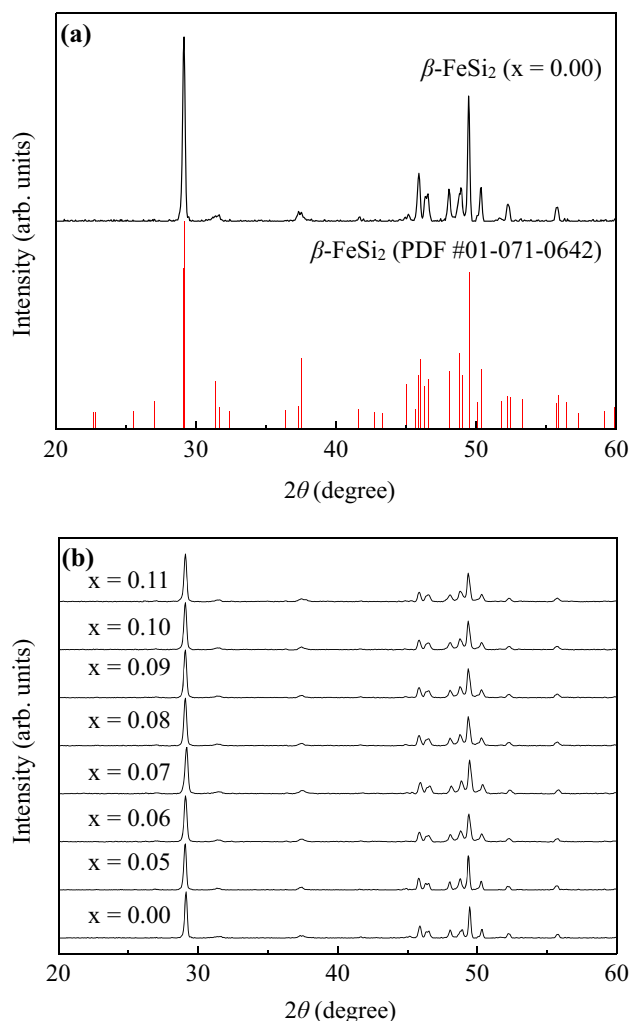


Fig. 1. XRD patterns of (a)  $\beta$ -FeSi<sub>2</sub> and (b) Co-doped  $\beta$ -FeSi<sub>2</sub> materials.

while the black region is a C-rich phase. The chemical composition suggests it is a SiC phase, although we cannot observe it by XRD. For the 5 wt.% sample, most of the SiC phases show a size around 100 nm to 200 nm and only a few large agglomerates are observed. Since the initial SiC nanoparticles possess an average size of 50 nm to 60 nm, the comparable SiC size observed in our samples indicates that we can disperse the nanoparticles into the matrix homogeneously without significant agglomeration by the current preparation procedure. On the other hand, all the SiC particles are isolated by the matrix material. This characteristic is helpful to suppress diffusion among the nanoparticles, thus the nano-inclusions will hardly coarsen during high-temperature operation.<sup>28</sup>

The temperature dependence of the electrical resistivity of the Co-doped  $\beta$ -FeSi<sub>2</sub> samples is shown in Figure 4. The pure  $\beta$ -FeSi<sub>2</sub> exhibited much higher resistivity than the doped samples. It has been reported that the resistivity of *n*-type doped  $\beta$ -FeSi<sub>2</sub> at low temperature (below 120 K) is consistent with

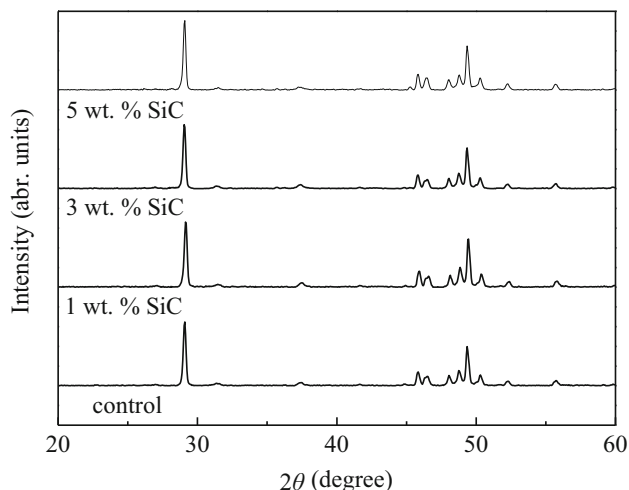
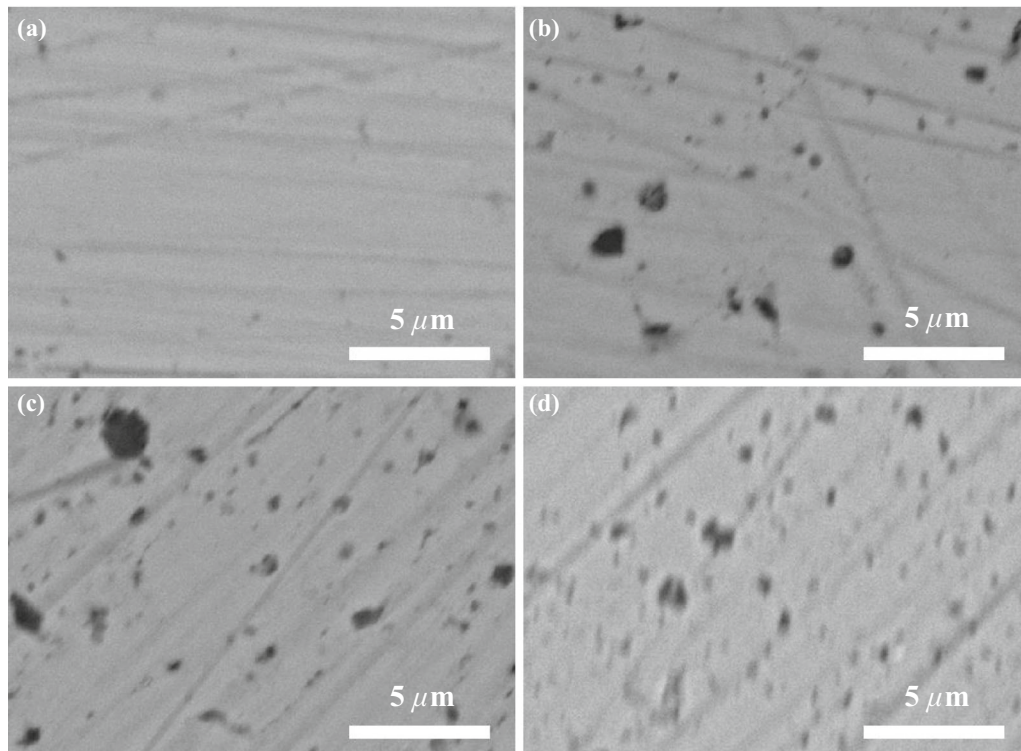


Fig. 2. XRD patterns of  $\beta$ -Fe<sub>0.92</sub>Co<sub>0.08</sub>Si<sub>2</sub>-SiC composites.

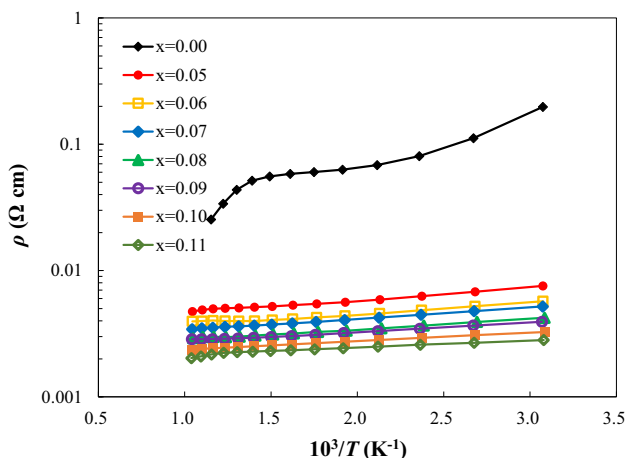
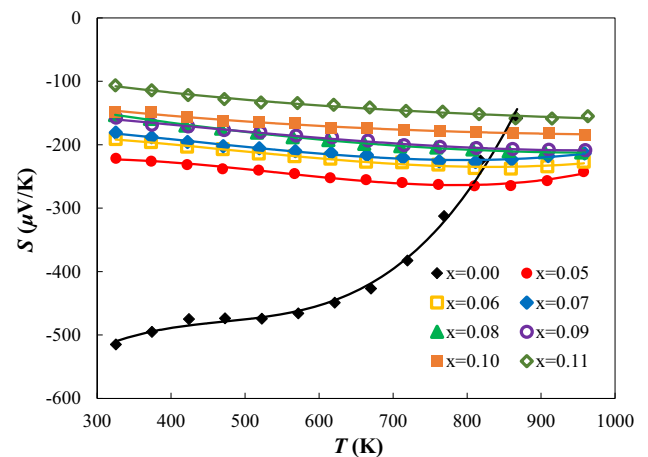
the variable-range hopping mechanism.<sup>29</sup> The resistivity of Co-doped  $\beta$ -FeSi<sub>2</sub> between 150 K and 900 K was also analyzed using the small-polaron hopping mechanism based on resistivity and Hall results.<sup>13,14,30</sup> We attempted to measure the carrier concentration and mobility of our samples. However, no convincing results were obtained because of the nonlinear behavior of the Hall resistance versus the magnetic field. Such deviation from a linear relation has been explained by two views: Arushanov et al. believed that the coexistence of light and heavy electrons resulted in the anomalous behavior,<sup>31</sup> while Lengsfeld et al. ascribed it to extrinsic magnetic clusters.<sup>32</sup> Returning to our results, the pure  $\beta$ -FeSi<sub>2</sub> still behaves like a slightly doped sample as its resistivity decreased obviously with increasing temperature below 400 K. This is presumably caused by the impurities in our starting materials or cobalt contamination from the tungsten carbide vial set (the same tungsten carbide vial set used in the current work was also used to prepare CoSi and  $\beta$ -FeSi<sub>2</sub>-CoSi composite materials in our previous studies). The resistivity drops off quickly at temperatures above 700 K, indicating that the intrinsic region has been reached. The resistivity decreases monotonically with rising cobalt content, presumably due to the increase of the electron concentration.

The temperature dependence of the Seebeck coefficient is presented in Fig. 5. The absolute Seebeck coefficient decreases with increasing doping level. This agrees with the variation of the resistivity and can also be attributed to the increasing carrier concentration. The Seebeck coefficient of  $\beta$ -FeSi<sub>2</sub> shows a negative sign over the entire temperature range. The undoped  $\beta$ -FeSi<sub>2</sub> is supposed to exhibit positive and smaller Seebeck coefficients in this temperature range according to previous studies.<sup>3</sup> Therefore, our  $\beta$ -FeSi<sub>2</sub> sample is slightly *n*-type doped, which agrees with the resistivity behavior. The Seebeck coefficient approaches


 Fig. 3. BSE images of (a)  $\beta$ -Fe<sub>0.92</sub>Co<sub>0.08</sub>Si<sub>2</sub> control sample, and (b) 1 wt.%, (c) 3 wt.%, and (d) 5 wt.% SiC composites.

**Table I. Chemical composition (at.%) of gray region and black region phases for samples in Fig. 3**

Sample	Grey Region			Black Region		
	Fe	Co	Si	Fe	Si	C
Control	28.83	2.34	68.83			
1 wt.% SiC	28.78	2.55	68.67	7.50	43.61	48.89
3 wt.% SiC	29.70	2.67	67.63	6.28	42.26	51.46
5 wt.% SiC	28.56	2.62	68.82	6.52	38.13	55.35


 Fig. 4. Electrical resistivity of Co-doped  $\beta$ -FeSi<sub>2</sub> samples versus reciprocal temperature. Solid lines are guides to the eye.

 Fig. 5. Temperature dependence of Seebeck coefficient of Co-doped  $\beta$ -FeSi<sub>2</sub> samples. Solid lines are guides to the eye.

zero quickly when the temperature is above 700 K, because of the opposite effect of the thermally excited holes on the Seebeck coefficient. Compared with  $\beta$ -FeSi<sub>2</sub>, the Co-doped samples exhibited increasing absolute Seebeck coefficients from 300 K to 700 K. This behavior has also been understood base on the small-polaron conduction mechanism.<sup>17,33</sup> This trend cannot be understood using the band conduction model for degenerate semiconductors as the Seebeck coefficient is much larger than that determined by band conduction.<sup>33</sup>

The power factor of the Co-doped  $\beta$ -FeSi<sub>2</sub> samples revealed a pronounced compositional dependence



(Fig. 6). The samples with  $x$  values in the range from 0.05 to 0.07 all exhibited a peak power factor of  $14 \mu\text{W K}^{-2} \text{cm}^{-1}$  at 850 K, while the highest power factor of the samples with  $x = 0.08$  and  $0.09$  occurred at 950 K and increased to  $15 \mu\text{W K}^{-2} \text{cm}^{-1}$ . A further increase of the cobalt concentration led to a decrease in the power factor.

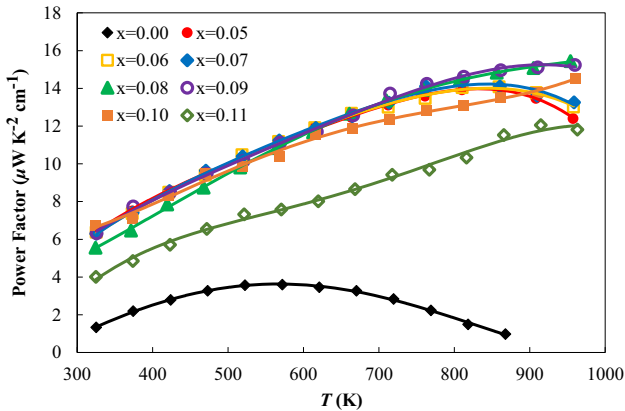


Fig. 6. Temperature dependence of power factor of Co-doped  $\beta$ - $\text{FeSi}_2$  samples. Solid lines are guides to the eye.

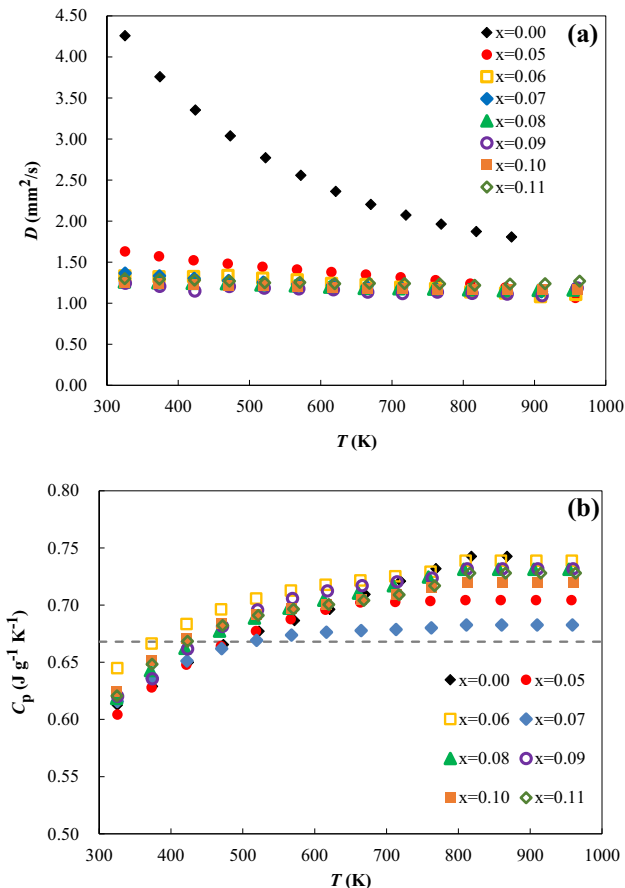


Fig. 7. High-temperature thermal transport measurements for Co-doped  $\beta$ - $\text{FeSi}_2$ : (a) thermal diffusivity and (b) specific heat capacity. The dashed line in (b) is the Dulong–Petit value.

The thermal diffusivity and specific heat capacity results are shown in Fig. 7a and b, respectively. It is clearly seen that the thermal diffusivity of the  $x = 0.00$  and  $0.05$  samples continued to decrease with increasing temperature. On the contrary, the variation of the thermal diffusivity was much flatter for the samples with higher cobalt concentrations, and it increased slightly at temperatures above 900 K. All the samples showed less difference in the specific heat capacity. Since the upper temperature limit for our differential scanning calorimetry (DSC) measurements was  $600^\circ\text{C}$ , the data were extrapolated assuming that the specific heat capacity was constant above 850 K. This assumption is quite reasonable because the reported Debye temperature for  $\beta$ - $\text{FeSi}_2$  is 630 K,<sup>19</sup> which is more than 200 K below the extrapolated onset. The  $C_p$  data for all the samples were larger than the Dulong–Petit value at temperatures above 600 K and even slightly higher than literature data.<sup>19</sup> Based on the thermal diffusivity and specific heat capacity data, the thermal conductivity was calculated using the room-temperature density of each sample. The thermal conductivity of all the samples is shown in Fig. 8a. Provided that the Co-doped  $\beta$ - $\text{FeSi}_2$  materials are degenerate semiconductors, the electronic thermal conductivity can be calculated using the

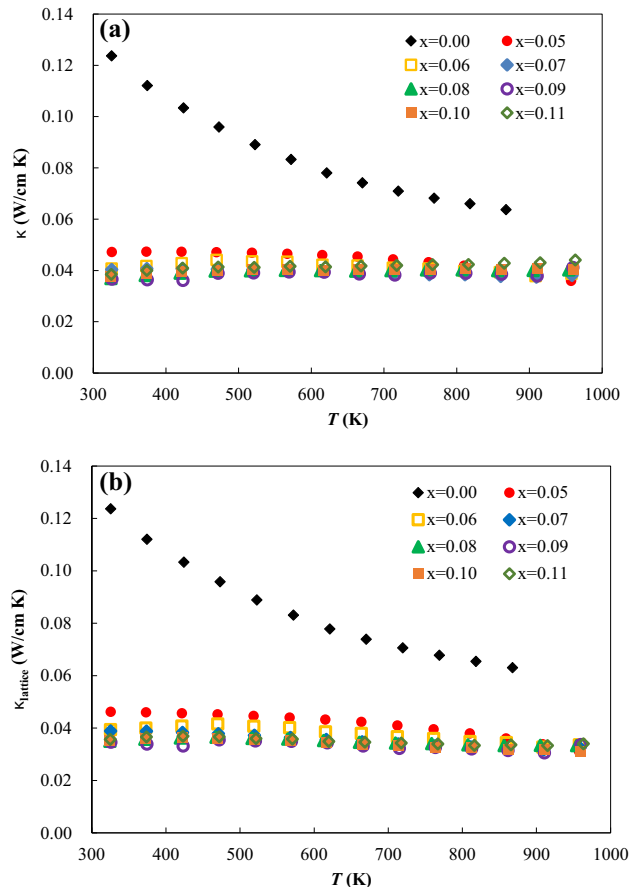


Fig. 8. Temperature dependence of (a) thermal conductivity and (b) lattice thermal conductivity of Co-doped  $\beta$ - $\text{FeSi}_2$  samples.

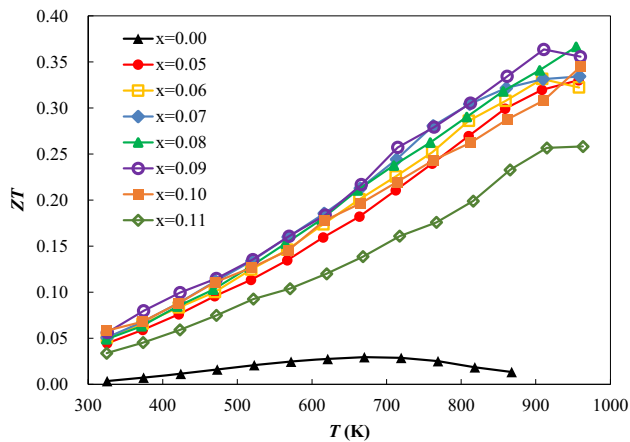


Fig. 9. Temperature dependence of  $ZT$  of Co-doped  $\beta$ -FeSi<sub>2</sub> samples. Solid lines are guides to the eye.

Wiedemann–Franz law with a Lorenz number of  $2.45 \times 10^{-8} \text{ J}^2 \text{ K}^{-2} \text{ C}^{-2}$ . The lattice thermal conductivity was calculated by subtracting the electronic contribution from the total thermal conductivity and is shown in Fig. 8b. The thermal conductivity increases slightly for the samples with  $x = 0.08$  to  $0.11$  around the highest temperature, presumably due to the increasing electronic thermal conductivity. It is noticeable that the thermal conductivity is drastically reduced by Co-doping. This reduction stems mainly from the lattice thermal conductivity. Point-defect scattering by cobalt should be very small due to its similar atomic weight and size to iron atoms. The drastic decrease in the lattice thermal conductivity is an interesting phenomenon because it can be ascribed to a strong electron–phonon interaction. This hypothesis can also be proposed based on the low carrier mobility and the possible small-polaron conduction for  $n$ -type doped  $\beta$ -FeSi<sub>2</sub> samples.<sup>15,17,34</sup>

Figure 9 shows the temperature dependence of  $ZT$ . The samples with  $x = 0.05$  to  $0.10$  showed comparable  $ZT$  values over the entire temperature range. Based on these results, the highest  $ZT$  of  $0.35$  at  $950 \text{ K}$  was obtained for Co-doped  $\beta$ -FeSi<sub>2</sub>. The best  $ZT$  occurs within a wide range of doping level, implying that an accurate doping concentration and high-purity starting materials are not required to achieve the best performance. In addition, the high doping concentration can also resist degradation induced by impurity diffusion during high-temperature operation.<sup>3</sup> All of these advantages are quite meaningful for practical applications of thermoelectric power generators.

According to the thermoelectric performance of the Co-doped  $\beta$ -FeSi<sub>2</sub> samples, the composition with  $x = 0.08$  was chosen as a control to further study the influence of the introduction of SiC nanoparticles into the matrix material. Figure 10 shows the thermoelectric properties of the composites and the control sample. The resistivity of all the SiC composites was slightly higher than that of the

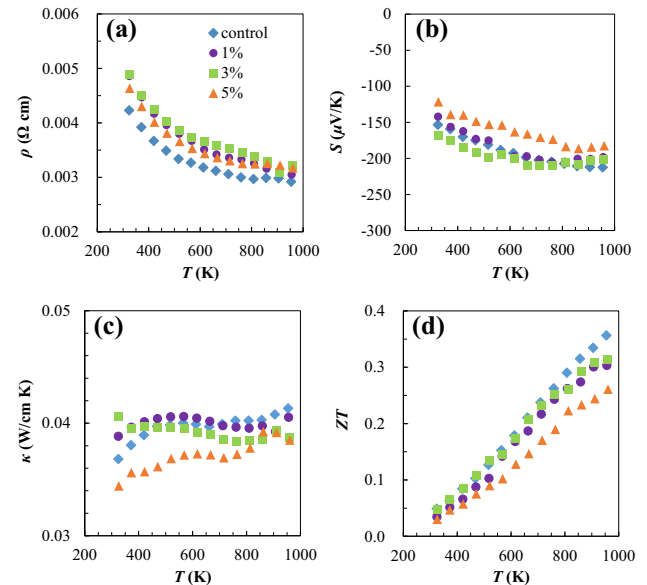


Fig 10. Temperature dependence of (a) electrical resistivity, (b) Seebeck coefficient, (c) thermal conductivity, and (d)  $ZT$  of the control sample and the SiC composites.

control sample, probably due to the high resistivity of the inclusions. It is interesting that the increase of the resistivity showed no clear dependence on the SiC concentration, and the increment was relatively small. This phenomenon probably indicates that the matrix material provides the main electrical conduction paths.<sup>35</sup> The Seebeck coefficient was not affected by addition of  $1 \text{ wt.}\%$  or  $3 \text{ wt.}\%$  SiC; however, the  $5 \text{ wt.}\%$  composite exhibited a lower Seebeck coefficient compared with the control. As mentioned above, SiC itself is an inert inclusion and hence should not affect the carrier concentration. The decrease of the Seebeck coefficient is likely caused by other reasons. In a study of Bi<sub>2</sub>Te<sub>3</sub>–SiC composites, Zhao et al. also found a similar change of the Seebeck coefficient.<sup>36</sup> They proposed that contamination from the oxidized surface of the SiC nanoparticles could decrease the Seebeck coefficient when the SiC concentration reached a certain amount.<sup>36</sup> SiC addition only induced a slight decrease in the thermal conductivity at high temperatures. As the electrical resistivity is increased, the partial decrease even stems from the reduction of the electronic contribution. This is consistent with the observation by Zhao et al.’s that the addition of  $1 \text{ vol.}\%$  SiC to Bi<sub>2</sub>Te<sub>3</sub> matrix even increased the thermal conductivity.<sup>36</sup> They attributed this behavior to the high thermal conductivity of SiC.<sup>36,37</sup> Furthermore, the variation of the thermal conductivity may also be influenced by the size of the inclusions. It has been pointed out that a critical size of around  $5 \text{ nm}$  is required for inclusions in Si<sub>0.8</sub>Ge<sub>0.2</sub> materials to scatter heat-carrying phonons.<sup>28,38</sup> The SiC size is approximately a few hundred nanometers in our study, and they are supposed to scatter long-wavelength phonons. If

most of the heat is carried by shorter-wavelength phonons, these large inclusions then cannot effectively reduce the thermal conductivity. Since the reduction of the thermal conductivity is less than the decrease of the power factor, no improvement is obtained for the composites.

## CONCLUSIONS

Single-phase Co-doped  $\beta$ -FeSi<sub>2</sub> materials can be prepared using sequential arc melting, ball milling, PECS, and annealing procedures. The highest  $ZT$  value of around 0.35 was obtained within quite a wide doping range at temperatures above 900 K. A composite structure consisting of a large grain matrix and well-isolated inert nanoinclusions may benefit the reduction of the thermal conductivity and thus further improve the thermoelectric properties. However, there is no significant improvement in  $ZT$  for  $\beta$ -Fe<sub>0.92</sub>Co<sub>0.08</sub>Si<sub>2</sub> and SiC composites. Since SiC is a high-thermal-conductivity material, the effect of inclusion scattering may be offset by this nature. It is worth trying other chemically stable inclusions with lower thermal conductivity. Some inert particles such as Si<sub>3</sub>N<sub>4</sub>, TiN, TiO<sub>2</sub>, ZrO<sub>2</sub>, etc. are possible candidates. These nanoparticles with size down to 20 nm can be readily obtained from commercial companies. Thus, more comprehensive understanding of the thermoelectric properties of nanocomposites could be established by investigating a number of inclusions with various average sizes.

## ACKNOWLEDGMENTS

This work is supported as part of the Center for Revolutionary Materials for Solid State Energy Conversion, an Energy Frontier Research Center funded by the US Department of Energy, Office of Science, Office of Basic Energy Sciences under Award Number DE-SC0001054, and we acknowledge the first author's dissertation work that is used in writing the manuscript. We also thank the sponsorship from the University Outstanding Talent Funding Project of Anhui Province under Project Number gxbjZD58 and the sponsorship from the Returned Scholars Innovation Supporting Plan of Anhui Province.

## CONFLICT OF INTEREST

The authors declare that they have no conflicts of interest.

## REFERENCES

1. G. Himm, and P.J. Klar, *Phys. Status Solidi-R* 5, 324 (2011).
2. S.W. Kim, M.K. Cho, Y. Mishima, and D.C. Choi, *Intermetallics* 11, 399 (2003).
3. R.M. Ware, and D.J. McNeill, *Proc. Inst. Electr. Eng.* 111, 178 (1964).
4. E. Arushanov, M. Respaud, J.M. Broto, C. Kloc, J. Leotin, and E. Bucher, *Phys. Rev. B* 53, 5108 (1996).
5. J. Chai, C. Ming, X. Du, P. Qiu, Y. Sun, and L. Chen, *Phys. Chem. Chem. Phys.* 21, 10497 (2019).
6. D.J. Oostra, C.W.T. Bullelieuwma, D.E.W. Vandenhoudt, F. Felten, and J.C. Jans, *J. Appl. Phys.* 74, 4347 (1993).
7. C. Giannini, S. Lagomarsino, F. Scarinci, and P. Castrucci, *Phys. Rev. B* 45, 8822 (1992).
8. S. Eisebitt, J.E. Rubensson, M. Nicodemus, T. Boske, S. Blugel, W. Eberhardt, K. Radermacher, S. Mantl, and G. Bihlmayer, *Phys. Rev. B* 50, 18330 (1994).
9. A.B. Filonov, D.B. Migas, V.L. Shaposhnikov, N.N. Dorozhkin, G.V. Petrov, V.E. Borisenko, W. Henrion, and H. Lange, *J. Appl. Phys.* 79, 7708 (1996).
10. V.N. Antonov, O. Jepsen, W. Henrion, M. Rebien, P. Stauss, and H. Lange, *Phys. Rev. B* 57, 8934 (1998).
11. R. Eppenga, *J. Appl. Phys.* 68, 3027 (1990).
12. Z. He, D. Platzek, C. Stiewe, H. Chen, G. Karpinski, and E. Mueller, *J. Alloys Compd.* 438, 303 (2007).
13. T. Kojima, *Phys. Status Solidi A* 111, 233 (1989).
14. J. Tani, and H. Kido, *J. Appl. Phys.* 84, 1408 (1998).
15. J. Tani, and H. Kido, *J. Appl. Phys.* 88, 5810 (2000).
16. S.L. Tonquesse, Z. Verastegui, H. Huynh, V. Dorcet, M. Pasturel, and A.C.S. Appl. *Energy Mater.* 2, 8525 (2019).
17. J. Tani, and H. Kido, *Jpn. J. Appl. Phys.* 40, 3236 (2001).
18. J. Hesse, and R. Bucksch, *J. Mater. Sci.* 5, 272 (1970).
19. G. Waldecke, H. Meinhold, and U. Birkholz, *Phys. Status Solidi A* 15, 143 (1973).
20. Y. Lan, A.J. Minnich, G. Chen, and Z. Ren, *Adv. Funct. Mater.* 20, 357 (2010).
21. N. Liu, S.E. Rezaei, W.A. Jensen, S. Song, Z. Ren, K. Esfarjani, M. Zebarjadi, and J.A. Floro, *Adv. Funct. Mater.* 29, 1903157 (2019).
22. X. Zianni, *J. Appl. Phys.* 126, 194301 (2019).
23. N. Nandihalli, C.J. Liu, and T. Mori, *Nano Energy* 78, 105186 (2020).
24. Q.S. Meng, W.H. Fan, R.X. Chen, and Z.A. Munir, *J. Alloys Compd.* 492, 303 (2010).
25. Y. Ohta, S. Miura, and Y. Mishima, *Intermetallics* 7, 1203 (1999).
26. Y.K. Hsu, J.J. Wang, C.S. Chang, and S.C. Wang, *Jpn. J. Appl. Phys.* 41, 3854 (2002).
27. K. Nogi, and T. Kita, *J. Mater. Sci.* 35, 5845 (2000).
28. N. Scoville, C. Bajgar, J. Rolfe, J.P. Fleurial, and J. Vandersande, *Nanostruct. Mater.* 5, 207 (1995).
29. E. Arushanov, K. Nenkov, D. Eckert, H. Vinzelberg, U.K. Rossler, G. Behr, K.H. Muller, and J. Schumann, *J. Appl. Phys.* 96, 2115 (2004).
30. U. Birkholz, and J. Schelm, *Phys. Status Solidi* 27, 413 (1968).
31. E. Arushanov, C. Kloc, H. Hohl, and E. Bucher, *J. Appl. Phys.* 75, 5106 (1994).
32. P. Lengsfeld, S. Brehme, G. Ehlers, H. Lange, N. Stusser, Y. Tomm, and W. Fuhs, *Phys. Rev. B* 58, 16154 (1998).
33. C. Wood, and D. Emin, *Phys. Rev. B* 29, 4582 (1984).
34. N.E. Christensen, *Phys. Rev. B* 42, 7148 (1990).
35. J.F. Li, W.S. Liu, L.D. Zhao, and M. Zhou, *NPG Asia Mater.* 2, 152 (2010).
36. L.D. Zhao, B.P. Zhang, J.F. Li, M. Zhou, W.S. Liu, and J. Liu, *J. Alloys Compd.* 455, 259 (2008).
37. G.A. Slack, *J. Appl. Phys.* 35, 3460 (1964).
38. D.P. White, and P.G. Klemens, *J. Appl. Phys.* 71, 4258 (1992).

**Publisher's Note** Springer Nature remains neutral with regard to jurisdictional claims in published maps and institutional affiliations.